Abdominal Radiology (2019) 44:3115–3126
https://doi.org/10.1007/s00261-019-02068-2

HEPATOBILIARY

Differentiation of hypervascular primary hepatic tumors showing hepatobiliary hypointensity on gadoxetic acid-enhanced magnetic resonance imaging

Hyun Jeong Park[1] · Young Kon Kim[2] · Ji Hye Min[3] · Jisun Lee[4] · Soon Jin Lee[2] · Eun Sun Lee[1] · Soohyun Ahn[5]

Published online: 27 May 2019

Abstract

Purpose To determine the imaging features that help differentiate hypervascular primary hepatic tumors showing hepatobiliary hypointensity on gadoxetic acid MRI.

Methods This study comprised 148 patients with pathologically proven hypervascular hepatic tumors who underwent gadoxetic acid MRI. Tumors included 23 atypical focal nodular hyperplasias (FNHs), 11 hepatocellular adenomas (HCAs), 15 neuroendocrine tumors (NETs), 25 intrahepatic cholangiocarcinomas (ICCs), and 74 hepatocellular carcinomas (HCCs). MRIs were analyzed for morphologic features, signal intensity, and enhancement pattern of the tumors to determine the differential features using multivariate logistic regression analysis. We evaluated the diagnostic performance of the MRI features for differentiating the five tumor types upon review by two observers.

Results Multivariate analysis revealed that reverse target sign on hepatobiliary phase in FNHs ($p = 0.009$), iso or hyperintensity on ADC map in FNHs and HCAs ($p = 0.009, < 0.001$, respectively), central hypointensity on arterial phase in NETs ($p = 0.001$), hepatobiliary target sign in ICCs ($p = 0.002$), the presence of septum and capsule in HCCs (all $p < 0.001$) were significant independent features of each tumor group over other tumor groups. Diagnostic accuracy for both observers was 98–98.6% for FNHs, 96.6–98% for HCAs, 97.3–98.6% for NETs, 90.5–94.6% for ICCs, and 85.8–93.2% for HCCs.

Conclusions Ancillary MRI features established in our study can be helpful in the differentiation of hypervascular and hepatobiliary hypointense primary hepatic tumors on gadoxetic acid MRI.

Keywords Gadoxetic acid · MRI · Hypervascular hepatic tumor · Ancillary feature

Introduction

Noninvasive characterization of hepatic tumors is largely based on their hemodynamic enhancement patterns on contrast-enhanced dynamic imaging. Gadoxetic acid (Gd-EOB-DTPA; Primovist, Bayer HealthCare, Berlin, Germany) allows us to receive hepatocyte functional information, as it offers early dynamic phases similar to those of extracellular agents as well as hepatobiliary phase (HBP) imaging [1, 2]. The advantage of this agent is its ability to delineate focal liver lesions as areas of hypointense defects against a strongly enhanced liver parenchyma on HBP, leading to improved sensitivity for hepatocellular carcinoma (HCC) diagnosis [3]. However, when applying hypointensity on transitional phase (TP) or HBP, erroneous diagnosis of non-HCC hypervascular hepatic tumors is a major concern because hepatocytes start uptake of gadoxetic acid, approximately, 60–90 s after contrast injection [4–10].

Electronic supplementary material The online version of this article (https://doi.org/10.1007/s00261-019-02068-2) contains supplementary material, which is available to authorized users.

✉ Young Kon Kim
youngkon0707.kim@samsung.com

[1] Department of Radiology, Chung-Ang University Hospital, Chung-Ang University College of Medicine, Seoul, Republic of Korea

[2] Department of Radiology and Center for Imaging Science, Samsung Medical Center, Sungkyunkwan University School of Medicine, 50, Ilwon-Dong, Kangnam-Ku, Seoul 135-710, Republic of Korea

[3] Department of Radiology, Chungnam National University Hospital, Chungnam National University College of Medicine, Daejeon, Republic of Korea

[4] Department of Radiology, Chungbuk National University Hospital, Cheongju, Republic of Korea

[5] Department of Mathematics, Ajou University, Suwon, Republic of Korea

With the increased use of imaging modalities, small focal liver lesions are more frequently detected on surveillance in patients with chronic liver disease [11]. This makes definitive diagnosis of small hypervascular hepatic tumors more difficult on the basis of conventional imaging features. For example, small intrahepatic cholangiocarcinomas (ICC) are more likely to show arterial hyperenhancement mimicking HCC than large ICC [9, 12]. In that sense, LI-RADS incorporates ancillary features to improve the confidence of HCC diagnosis by differentiating it from ICC (http://www.acr.org/Quality-Safety/Resources/LIRADS).

Several recent studies have shown the additional value of adding histomorphologic features to enhancement patterns in the diagnosis of HCC to differentiate it from ICC [9, 13–15]. With this concept in mind, we conducted this study to identify imaging features that facilitate differentiation of hypervascular primary hepatic tumors showing HBP hypointensity on gadoxetic acid MRI.

Materials and methods

Study population

The study is a retrospective case–control study at a single tertiary center. Our institutional review board approved this retrospective study and informed consent was waived. Using pathologic data, we searched non-HCC primary hepatic tumors with histologic confirmation between January 2012 and January 2016. This search identified 182 consecutive patients who had undergone gadoxetic acid-enhanced liver MRI. Of those patients, 108 were excluded from the study as tumors showed either arterial non-hyperenhancement ($n=67$) or HBP non-hypointensity ($n=41$). Arterial hyperenhancement and hypointensity on HBP were defined as a hyperenhanced or hypointense tumor area relative to liver parenchyma was > 70% of the total area of the tumor in consideration of tumor heterogeneity. Finally, 23 atypical focal nodular hyperplasias (FNHs), 11 hepatocellular adenomas (HCAs), 15 neuroendocrine tumors (NETs), and 25 ICCs met the inclusion criteria. To balance the study samples between HCCs and non-HCCs, we selected 74 consecutive patients with 74 surgically confirmed HCCs that showed arterial hyperenhancement and HBP hypointensity during the same inclusion period. A total of 148 consecutive patients (96 men, 51 women; age range 26–75 years; mean age, 57.7 years) were included. Diagnosis was made by surgery or percutaneous biopsy. Among the HCCs, 5 tumors were scirrhous HCCs. The detailed demographic data of the study groups are summarized in Table 1.

MRI acquisition

A 3-T whole-body MRI system (Intera Achieva 3.0 T; Philips Healthcare, Best, Netherlands) with a 32-channel phased-array (Torso/Cardiac, Philips Healthcare) receiver coil

Table 1 Demographic and pathologic characteristics

Characteristics	FNH	HCA	NET	ICC	HCC[a]
No. of patients	23	11	15	25	74
Male/female	6/17	1/10	9/6	19/6	62/12
Mean age (years)	43.5 ± 12.5	42.5 ± 13.1	58 ± 11.4	57.3 ± 10.2	60.7 ± 10.7
Underlying liver disease					
Hepatitis B	3	1	1	17	62
Hepatitis C	0	0	0	1	2
Unknown	20	10	14	7	10
Cirrhosis/fibrosis	0	1	2	12	69
Pathology (no. of tumors)					
Biopsy	10	1	6	0	0
Surgical resection	13	10	9	25	74
Tumor grade I/II/III/IV[†]	NA	NA	NA	NA	2/59/12/1
Capsule/septum	0/1	6 (1[b])/2	4 (2[b])/0	1/3	69 (11[b])/68
Tumor size (cm)					
Mean	2.3 ± 1.3	3.7 ± 1.9	3.0 ± 2.5	3.0 ± 1.3	2.8 ± 1.0
Range	1.2–6	1.1–8	1.2–10	1.2–6	1.3–6

FNH focal nodular hyperplasia, *HCA* hepatocellular adenoma, *NET* neuroendocrine tumor, *ICC* intrahepatic cholangiocarcinoma, *HCC* hepatocellular carcinoma, *NA* not applicable

[†]Edmondson–Steiner's grade

[a]Five lesions proved to be scirrhous HCC

[b]Numbers in parentheses for capsule include partial capsule

were used in this study. The MRI protocol is summarized in Table E1 (online). Diffusion-weighted imaging (DWI) was performed before the administration of gadoxetic acid using respiratory-triggered single-shot echo planar imaging with *b* values of 0, 100, and 800 s/mm^2. The apparent diffusion coefficient (ADC) was calculated using a monoexponential function with *b* values of 100 and 800 s/mm^2. For gadoxetic acid-enhanced MRI, unenhanced, enhanced arterial phase (AP) (20–35 s), PVP (70 s), 3-min TP, and 20-min HBP were obtained using a T1-weighted 3D turbo field-echo sequence (THRIVE [T1 high-resolution isotropic volume examination]; Philips Healthcare). The timing for the AP was determined using MR fluoroscopic bolus detection. A dose of 0.1 mL/kg (0.025 mmol/kg) of gadoxetic acid was administered intravenously at a rate of 1 mL/s using a power injector, followed by a 20-mL saline flush.

Image analysis

Image review consisted of two sessions. In the first session, the MRI was retrospectively and independently reviewed on a commercial workstation with a 2000 × 2000 PACS monitor (Centricity; GE Healthcare) by two abdominal radiologists (H.J.P. and Y.K.K. with 12 and 17 years of experience in liver MRI interpretation, respectively). Reviewers were unaware of the pathological diagnosis of tumors.

The MRI features evaluated for each tumor are summarized in Table 2. Reverse target signs consisted of a wide, central, hypointense area and a peripheral, thin, hyperintense rim on HBP (Fig. 1) [16–19]. Septum was defined as an intratumoral linear structure that completely divided the tumor into more than two compartments including mosaic architecture (Fig. 2) [20, 21]. For capsular appearance, along with enhancing capsules, we also considered nonenhancing capsule seen as hypointense on nonenhanced or contrast-enhanced T1-weighted images (T1WI), variable signal intensity on T2-weighed images (T2WI), and DWI [22]. Before image review, reviewers attended a training session in which imaging features were illustrated with representative cases not included in the study. After independently evaluating the images, the two observers jointly evaluated their results until a consensus was reached.

In the second session, two other observers (J.H.M. and J.L., with 10 and 8 years of experience, respectively)

Table 2 Definition of MRI features

Imaging features	Definition	κ value
Morphologic features		
Shape	Globular	0.742
	Non-globular, lobulated	
Intratumoral fat	Signal drop in out-of-phase imaging within tumors compared with signal intensity on in-phase imaging	0.952
Septum (Fig. 2a, PVP)	An intratumoral linear structure that completely divides the lesion into more than two compartments	0.704
Capsule (Fig. 2a, PVP)	Peripheral rim of smooth hyperenhancement in the portal venous phase or delayed phase or nonenhancing capsule on T1- and T2WI, and HBP	0.711
Biliary dilatation	Biliary obstruction disproportionate to that expected based on the size of the mass	0.781
T1WI		
Hyperintensity	Signal intensity of tumor higher than that of liver parenchyma	0.913
T2WI		
Hyperintense foci	At least three clustered, discrete, spotty or tubular bright foci within the hepatic tumor on T2WI	0.878
Hypointense area	Area with lower signal intensity than that of the liver parenchyma, suggesting fibrosis	0.775
DWI		
Target sign ($b = 800$) (Fig. 5b, DWI)	Central hypointense area and a peripheral hyperintense rim	0.849
ADC		
Iso to hyperintensity		0.901
Arterial phase		
Central hypointensity (Fig. 4a, AP)	Central area with lower signal intensity than tumor overall	0.867
HBP		
Target sign on HBP (Fig. 5a, HBPI)	Central enhancement less than surrounding liver parenchyma and a peripheral hypointense rim	0.830
Reverse target sign (Fig. 1a, HBP)	A central hypointense area and a peripheral hyperintense rim	0.902

PVP portal venous phase, *T1WI* T1-weighted images, *T2WI* T2-weighted imaging, *DWI* diffusion-weighted imaging, *HBP* hepatobiliary phase, *FNH* focal nodule hyperplasia, *HCA* hepatocellular adenoma, *NET* neuroendocrine tumor, *ICC* intrahepatic cholangiocarcinoma, *HCC* hepatocellular carcinoma

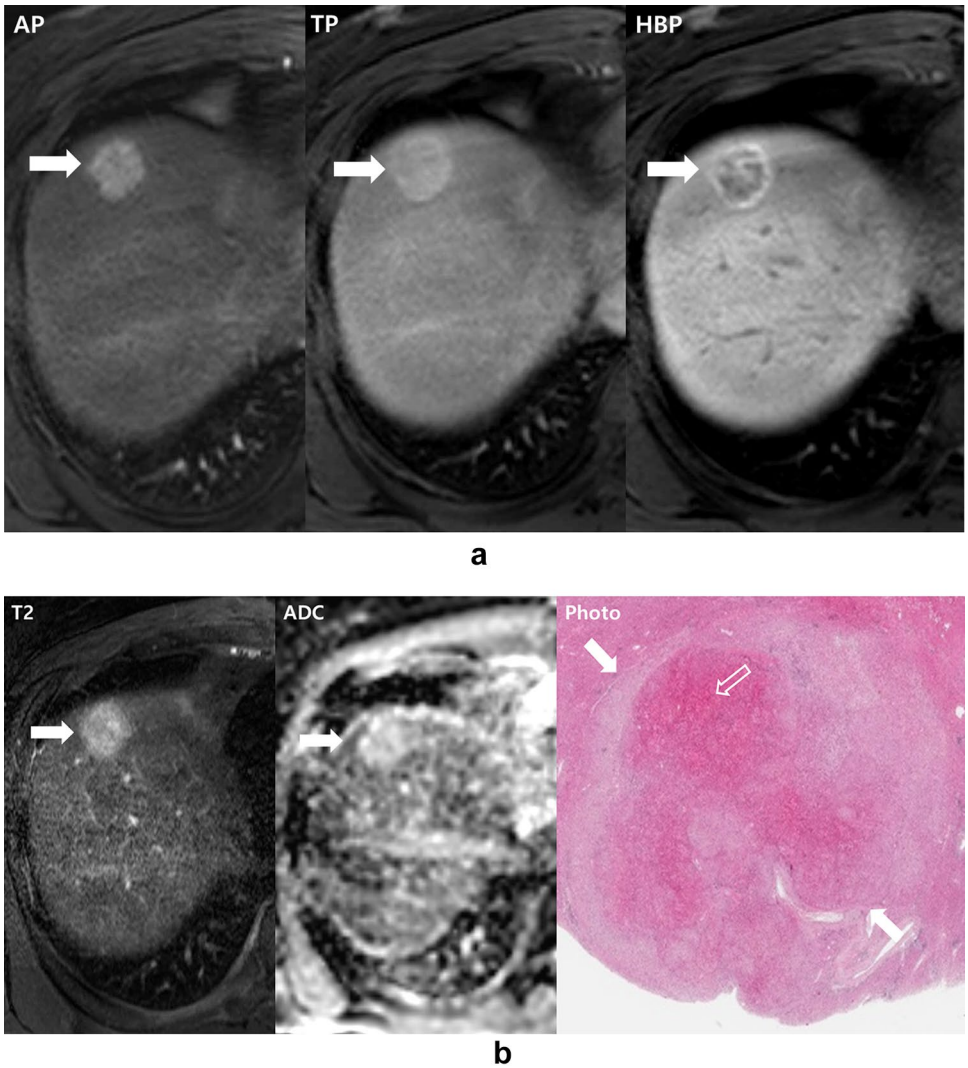

Fig. 1 Focal nodular hyperplasia in a 37-year-old woman. On arterial phase (**a**, AP) and 3-min transitional phase (**a**, TP) imaging after gadoxetic acid administration, the tumor shows arterial hyperenhancement with persistent enhancement. 20-min hepatobiliary phase imaging (**a**, HBP) reveals reverse target sign consisting of a central hypointense area with a thin hyperintense rim. The tumor shows diffuse hyperintensity on breath-hold multishot T2-weighted imaging (**b**, T2) and a high apparent diffusion coefficient value (**b**, ADC). A photomicrograph (**b**, Photo) shows the tumor (arrows) with wide central area of congestion (empty arrow) (Hematoxylin and Eosin staining; original magnification, × 1)

independently reviewed MRIs with regard to tumor classification. While the reviewers were aware of the purpose of this study, they were blinded to the results of the first session and information obtained by clinical and histopathological analyses. All of the images were mixed together and read in a nonselected order, without any access to patient identification. With emphasis on MRI features determined by uni- and multivariate analysis, two observers were asked to make optimal diagnoses among the five tumors. When lesions showed multiple ancillary features conflicting each other, preference was given to multiplicity or clarity of ancillary features for one tumor compared with the other.

Statistical analysis

The Kruskal–Wallis test and Chi-square test were applied to investigate intergroup differences of clinical and tumor characteristics including sex distribution, underlying liver disease, and tumor size. When the overall differences were statistically significant, post hoc analysis was performed for multiple comparisons among tumor groups. To determine independent, reliable findings to differentiate the tumor groups, multivariate logistic regression analysis was conducted with stepwise selection using significant variables on univariate regression analysis. The variables ($p < 0.1$) obtained from univariate regression analysis were used to conduct multivariable logistic regression analysis to determine the most reliable way to differentiate the five tumor groups. To avoid multicollinearity, we used a variance index factor and excluded variables with a factor greater than 10. Diagnostic accuracy, sensitivity, specificity, positive predictive value (PPV), and negative predictive value (NPV) were calculated for each observer for differentiation of the five tumor groups. Inter-observer agreement for each tumor differentiation was analyzed using kappa statistics and interpreted: less than 0.00 indicated poor agreement, 0.00–0.20, slight agreement; 0.21–0.40, fair agreement; 0.41–0.60,

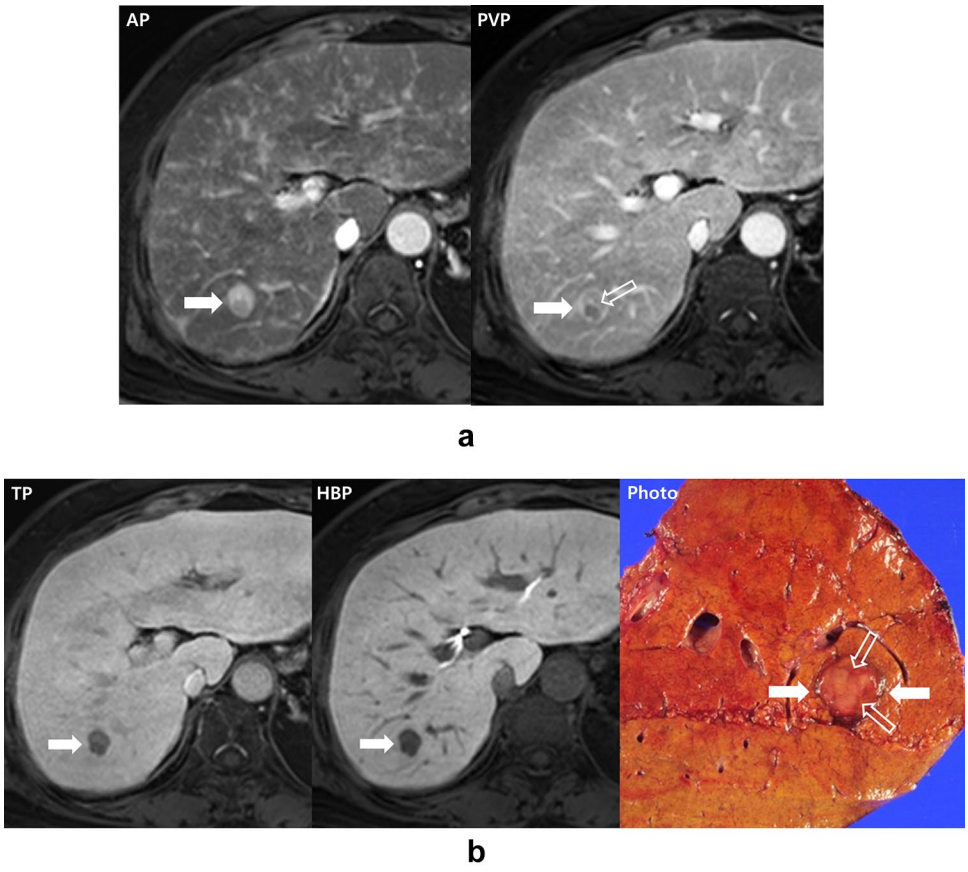

Fig. 2 Hepatocellular carcinoma in a 58-year-old man. On arterial phase (**a**, AP), portal venous phase (**a**, PVP), 3-min transitional phase (**b**, TP), and 20-min hepatobiliary phase imaging (**b**, HBP) after gadoxetic acid administration, the tumor is globular in shape and shows arterial hypervascularity and delayed washout. Capsular enhancement (arrow) and internal septum (empty arrow) appear on portal venous phase (**a**, PVP). A photograph of the resected specimen (**b**, Photo) shows a well-circumscribed, globular, solid mass with capsule (arrows) and intratumoral septa (empty arrows)

moderate agreement; 0.61–0.80, substantial agreement; and 0.81–1.00 excellent agreement.

In addition, the classification tree analysis (CTA) was determined based on conditional inference through a recursive partitioning procedure and a diagnostic category for differentiating the tumor groups was developed. Sensitivity, specificity, and diagnostic accuracy of the CTA were calculated for each hypervascular tumor. CTA was performed using the package 'party' and 'randomForest' in R 3.2.1 (Vienna, Austria; http://www.R-project.org/). All other statistical analysis was performed using SAS version 9.1.3 (SAS Inc., Cary, NC, USA).

Results

Study populations and tumor characteristics are shown in Table 1. The hypervascular tumor groups had a similar age distribution. Patients with FNHs and HCAs were predominantly female compared to other groups ($p < 0.001$). Underlying chronic liver disease was more frequently identified in ICC and HCC groups than those of other groups ($p < 0.001$). Lesion diameter was significantly larger in the HCA group (3.7 ± 1.9 cm) and smaller in FNH group (2.3 ± 1.3 cm) than those of other groups ($p = 0.001$). Pathologically, capsule was observed in 69 (93.2%) and septum in 68 (91.9%) of 74 HCCs. Reviewing surgically resected FNHs or HCAs, abundant sinusoidal dilatation or congestion was shown in the central area of the tumors, which in turn was seen as a collapsed central area of the cut surface on gross specimens. NET exhibited central fibrosis on pathology.

Image analysis

For differentiation of hypervascular tumor groups, the results of univariate logistic regression of evaluated MRI features in the first reading session are summarized in Table 3. Statistically significant parameters of each hypvervascular tumor group on univariate analysis are as follows: septum ($p = 0.002$), iso to hyperintensity on ADC maps ($p < 0.001$), central hypointensity on AP ($p = 0.014$), persistent hyperintensity on PVP and TP (all $p < 0.001$), and reverse target sign on HBP ($p < 0.001$) in the FNH group; intratumoral fat ($p = 0.036$), hyperintensity on T1WI ($p = 0.002$), iso to hyperintensity on ADC map ($p < 0.001$), and isointensity on TP ($p = 0.011$) in the HCA group; absence of septum ($p = 0.024$), hypointense area on T2WI ($p = 0.021$) and central hypointensity on AP ($p < 0.001$) in the NET group; non-globular shape ($p < 0.001$), biliary dilatation ($p = 0.031$), hypointense area on T2WI ($p < 0.001$), target sign on DWI

Table 3 Univariate logistic regression of MRI features for differentiation of hypervascular tumor groups

	FNH ($n=23$)	HCA ($n=11$)	NET ($n=15$)	ICC ($n=25$)	HCC ($n=74$)
Globular shape	17 (73.9)	9 (81.8)	7 (46.7)	3 (12)[a]	61 (82.4)[a]
Intratumoral fat	0	2 (18.2)[a]	0	0	4 (5.4)
Septum	1 (4.3)[a]	2 (18.2)	0[a]	0	59 (79.7)[a]
Capsule	0	6 (54.5)	4 (26.7)[b]	0	62 (83.8)[a]
Biliary dilatation	0	0	0	3 (12)[a]	2 (2.7)
SI on T1WI					
High	1 (4.3)	4 (36.4)[a]	0	0	0
Iso	2 (8.7)	0	0	0	8 (10.8)
Low	20 (87)	7 (63.6)	15 (100)	25 (100)	66 (89.2)
Hyperintense foci on T2WI	0	1 (9.1)	0	0	10 (13.5)[a]
Hypointense area on T2WI	1 (4.3)	0	7 (46.7)[a]	13 (52)[a]	11 (14.9)[b]
SI on DWI					
High	23 (100)	11 (100)	11 (73.3)	6 (24)	65 (87.8)[a]
Target sign	0	0	4 (26.7)	19 (76)[a]	9 (12.2)
SI on ADC					
High	18 (78.3)[a]	7 (63.6)[a]	2 (13.3)	0	0
Iso	5 (21.7)[a]	3 (27.3)[a]	0	0	1 (1.4)
Low	0	1 (9.1)	13 (86.7)	25 (100)[b]	73 (98.6)[a]
Central hypointensity on AP	2 (8.7)[a]	1 (9.1)	14 (93.3)[a]	4 (16)[a]	10 (13.5)[a]
SI on PVP					
High	22 (95.7)[a]	6 (54.5)[b]	5 (33.3)	4 (16)	8 (10.8)
Iso	6 (26.1)	3 (27.3)	3 (20)	6 (24)	12 (16.2)
Low	1 (4.3)	2 (18.2)	7 (46.7)	15 (60)	54 (73.0)[a]
SI on TP					
High	18 (78.3)[a]	0	0	1 (4)	0
Iso	3 (13)	6 (54.5)[a]	3 (20)	7 (28)	6 (8.1)
Low	2 (8.7)	5 (45.5)	12 (80)	17 (68)	68 (91.9)[a]
SI on HBP					
Iso	0	0	0	0	2 (2.7)
Low	4 (17.4)	11 (100)	9 (60)	3 (12)	67 (90.5)[a]
Target sign	0	0	6 (40)	21 (84)[a]	5 (6.8)
Reverse target sign	19 (82.6)[a]	0	0	0	0

Data are presented as the number of tumors with the percentage in parentheses

SI signal intensity, *T1WI* T1-weighted imaging, *T2WI* T2-weighted imaging, *DWI* diffusion-weighted imaging, *ADC* apparent diffusion coefficient, *AP* arterial phase, *PVP* portal venous phase, *TP* transitional phase, *HBP* hepatobiliary phase, *FNH* focal nodule hyperplasia, *HCA* hepatocellular adenoma, *NET* neuroendocrine tumor, *ICC* intrahepatic cholangiocarcinoma, *HCC* hepatocellular carcinoma

[a] $p<0.05$

[b] $p<0.1$

($p<0.001$) and HBP ($p<0.001$), and central hypointensity on AP ($p<0.001$) in the ICC group; globular shape ($p<0.001$), presence of a septum ($p<0.001$) and capsule ($p<0.001$), hyperintense foci on T2WI ($p=0.025$), hyperintensity on DWI ($p=0.014$) and hypointensity on ADC maps, PVP, TP, and HBP (all $p<0.001$), and central hypointensity on AP ($p<0.001$) in the HCC group.

Multivariate logistic regression analysis (Table 4) revealed significant and independent variables differentiating each tumor group over other tumor groups. Each MRI parameter was as follows: iso or hyperintensity on ADC map (23/23, 100%) and reverse target sign on HBP (19/23, 82.6%) for the FNH group ($p=0.009$) (Fig. 1), iso or hyperintensity on ADC maps (10/11, 90.9%) in the HCA group ($p<0.001$) (Fig. 3), central hypointensity on AP (14/15, 93.3%) in the NET group ($p<0.001$) (Fig. 4), target sign on HBP (21/25, 84%) in the ICC group ($p=0.002$) (Fig. 5), and the presence of a septum (59/74, 79.7%) and capsule (62/74, 83.8%) in the HCC group ($p<0.001$) (Fig. 2).

Table 4 Multivariate logistic regression of MRI features for differentiation of hypervascular tumor groups

	FNH		HCA	NET	ICC	HCC	
Independent parameter	Iso/hyper on ADC	Reverse target on HBPI	Iso/hyper on ADC	Central hypo on AP	Target sign on HBPI	Septum	Capsule
Estimate	4.5067/3.6159	4.8537	4.4048/4.1921	3.2139	2.6796	3.3799	2.2018
Standard error	1.479/1.4642	1.5981	1.4089/1.0573	0.884	0.7218	0.6611	0.5545
P value	0.009	0.009	< 0.001	< 0.001	0.002	< 0.001	< 0.001

FNH focal nodular hyperplasia, *HCA* hepatocellular adenoma, *NET* neuroendocrine tumor, *ICC* intrahepatic cholangiocarcinoma, *HCC* hepatocellular carcinoma, *SI* signal intensity, *ADC* apparent diffusion coefficient, *AP* arterial phase, *HBPI* hepatobiliary phase imaging

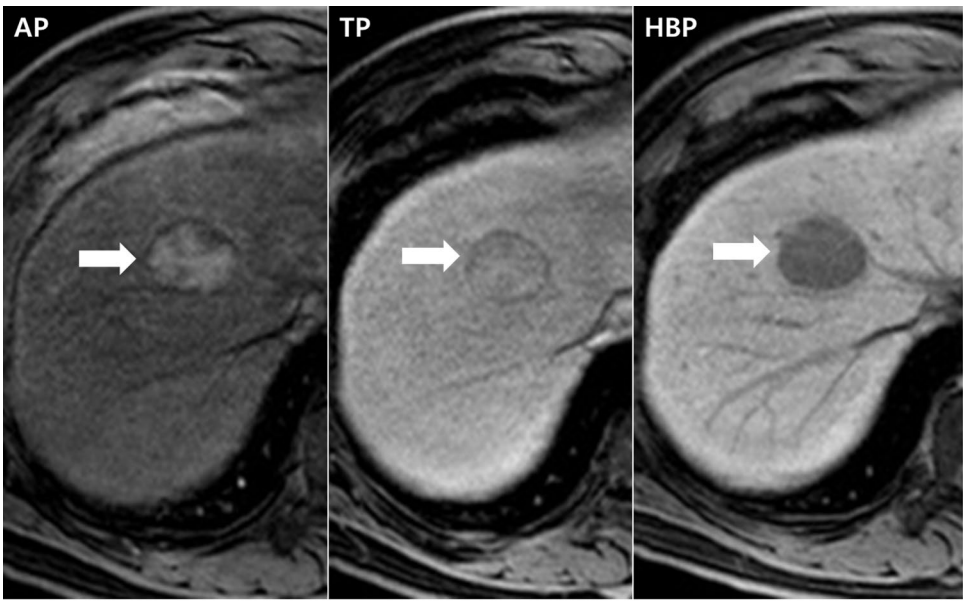

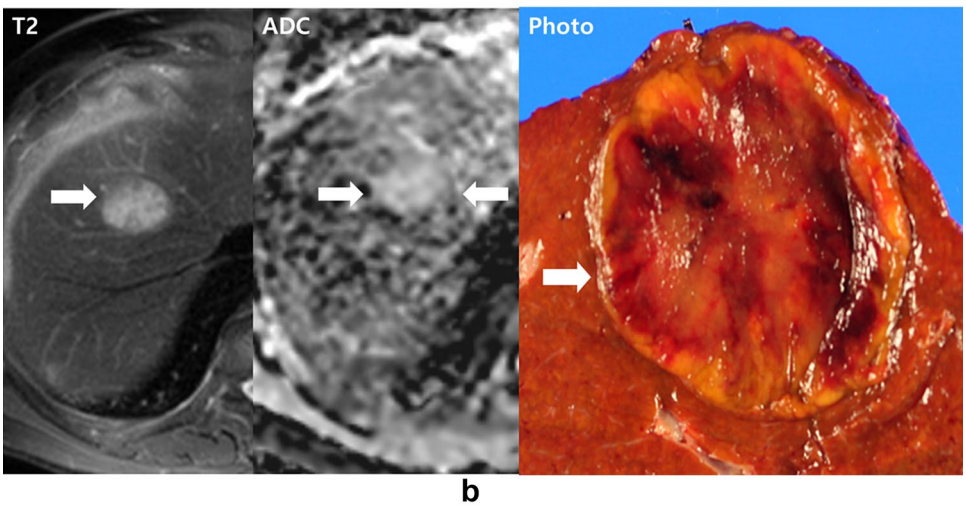

Fig. 3 Hepatocellular adenoma in a 42-year-old woman. On arterial phase (**a**, AP), 3-min transitional phase (**a**, TP), and 20-min hepatobiliary phase imaging (**a**, HBP) after gadoxetic acid administration, the tumor shows early hyperenhancement with nonenhancing capsule followed by isointensity (**a**, TP) and hypointensity (**a**, HBP). The tumor shows hyperintensity on breath-hold multishot T2-weighted imaging (**b**, T2) and a high apparent diffusion coefficient value (**b**, ADC). A photograph of the resected specimen (**b**, Photo) reveals a well-demarcated, globular mass (arrow) with capsule. Note that the central area of the tumor is collapsed due to loss of blood in the sinusoidal space

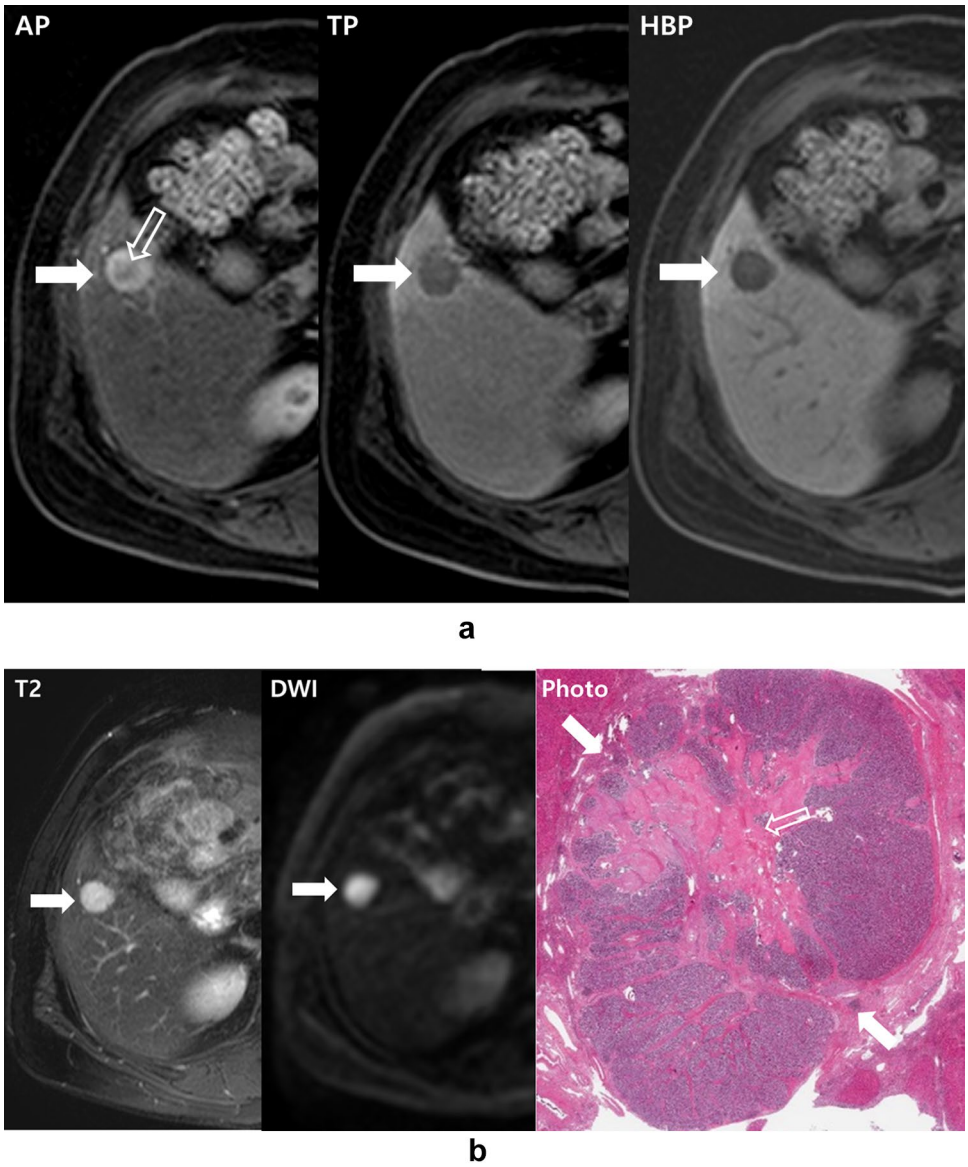

Fig. 4 Neuroendocrine tumor in a 47-year-old woman. On arterial phase (**a**, AP), 3-min transitional phase (**a**, TP), and 20-min hepatobiliary phase imaging (**a**, HBP) after gadoxetic acid administration, the tumor (arrows) shows arterial hyperenhancement with central hypointensity (empty arrow) (**a**, AP) followed by hypointensity. The tumor exhibits hyperintensity on breath-hold multishot T2-weighted imaging (**b**, T2) and restricted diffusion ($b = 800$) (**b**, DWI). A photomicrograph of the microscopic specimen (**b**, Photo) shows the tumor (arrows) with central fibrosis (empty arrow) (Hematoxylin and Eosin staining; original magnification, × 1)

Diagnostic performance and inter-observer agreement for differentiation of hypervascular tumor groups

The sensitivity, specificity, accuracy, PPV and NPV of the two observers in the second reading session for diagnosis of each hypervascular tumor group are presented in Table 5. The diagnostic accuracy for both observers was 98–98.6% in the FNH group, 96.6–98% in the HCA group, 97.3–98.6% in the NET group, 90.5–94.6% in the ICC group, and 85.8–93.2% in the HCC group. Both observers had six cases in common misdiagnosed as HCCs (1 NET, 2 HCAs, and 3 ICCs), and these tumors exhibited no capsule or septum on retrospective review. Of 74 HCCs, 3 tumors were misclassified as ICCs by both observers. Among them, two HCCs exhibited septum and capsule, and the other was a scirrhous HCC with neither septum nor capsule on retrospective review.

The κ value between the two observers was 0.832 for diagnosis of hypervascular tumor groups, indicating excellent inter-observer agreement.

Classification tree analysis for differentiating hypervascular tumor groups

The CTA for each tumor was determined by cross-validation error estimation with different nodes (Fig. 6). The first splitting imaging feature used to assess the differentiation of each hypervascular tumor was reverse target sign in FNH, iso to hyperintensity on T1WI in HCA, central hypointensity on

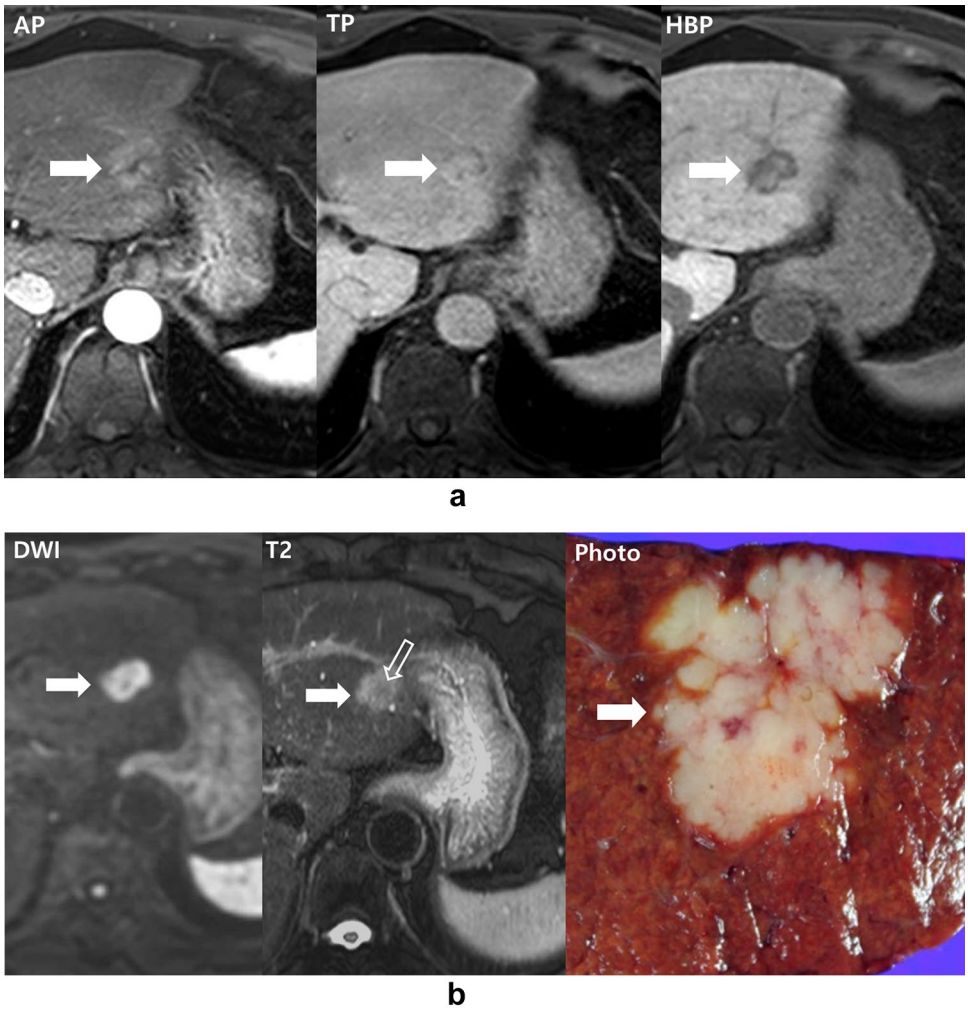

Fig. 5 Intrahepatic cholangiocarcinoma in a 54-year-old man. On arterial phase (**a**, AP), 3-min transitional phase (**a**, TP), and 20-min hepatobiliary phase imaging (**a**, HBP) after gadoxetic acid administration, the tumor is lobulated in shape (arrows) and shows arterial hyperenhancement with central hypointensity. The tumor shows target sign on both on hepatobiliary phase (**a**, HBP) and diffusion-weighted imaging ($b=800$) (**b**, DWI). Breath-hold multishot T2-weighted imaging (**b**, T2) reveals central hypointensity (empty arrow) indicating fibrous stroma. A photograph of the resected specimen (**b**, Photo) shows a well-demarcated, lobulated, whitish-tan, firm mass with central fibrotic tissue

Table 5 Diagnostic performance for differentiation of hypervascular tumor groups by two observers

	Sensitivity	Specificity	Accuracy	PPV	NPV
Observer 1					
FNH	91.3 (21/23)	100 (125/125)	98.6 (146/148)	100 (21/21)	99.2 (125/126)
HCA	72.7 (8/11)	100 (137/137)	98.0 (145/148)	100 (8/8)	98.6 (137/139)
NET	80.0 (12/15)	99.2 (132/133)	97.3 (144/148)	92.3 (12/13)	98.5 (132/134)
ICC	64.0 (16/25)	95.9 (118/123)	90.5 (134/148)	76.2 (16/21)	93.7 (118/126)
HCC	93.2 (69/74)	78.4 (58/74)	85.8 (127/148)	82.1 (69/84)	92.1 (58/63)
Observer 2					
FNH	87 (20/23)	100 (125/125)	98.0 (145/148)	100 (20/20)	98.4 (125/127)
HCA	81.8 (9/11)	97.8 (134/137)	96.6 (143/148)	75.0 (9/12)	99.3 (134/135)
NET	86.7 (13/15)	100 (133/133)	98.6 (146/148)	100 (13/13)	99.3 (133/134)
ICC	88.0 (22/25)	95.9 (118/123)	94.6 (140/148)	81.5 (22/27)	98.3 (118/120)
HCC	94.6 (70/74)	91.9 (68/74)	93.2 (138/148)	93.3 (70/75)	94.4 (68/72)

Data are presented as the percentage (no./total)

FNH focal nodule hyperplasia, *HCA* hepatocellular adenoma, *NET* neuroendocrine tumor, *ICC* intrahepatic cholangiocarcinoma, *HCC* hepatocellular carcinoma, *PPV* positive predictive value, *NPV* negative predictive value

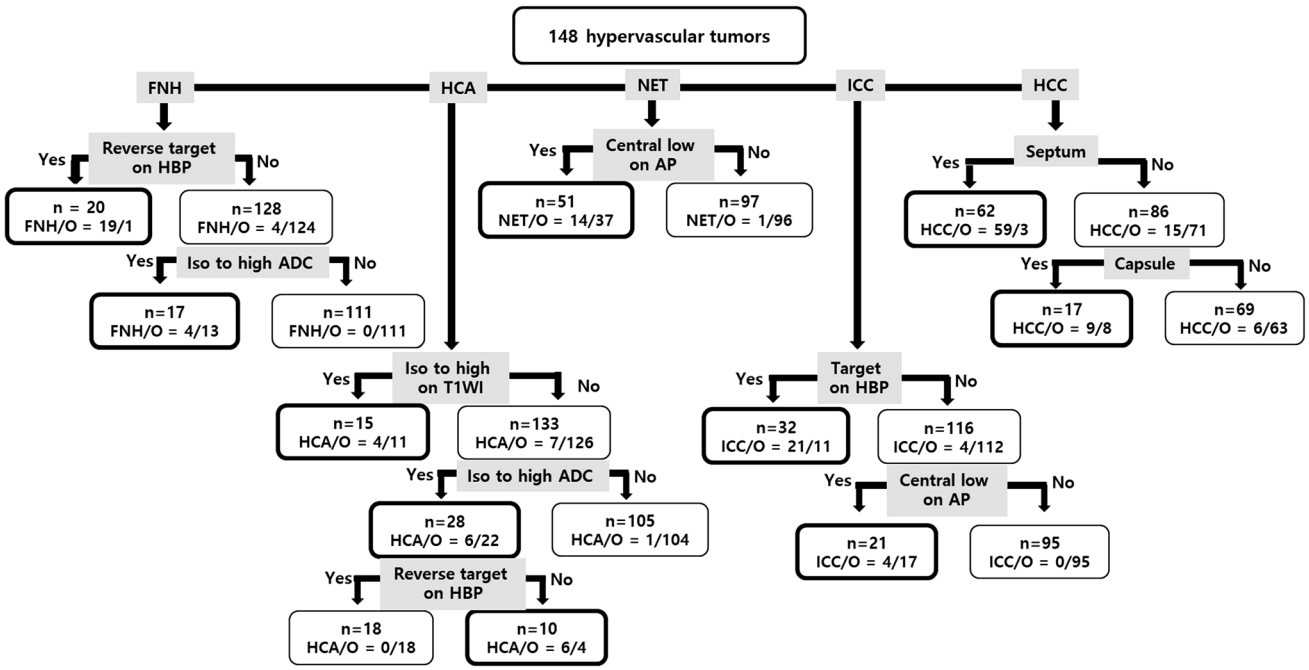

Fig. 6 Classification tree analysis for differentiating hypervascular tumors. *O* other tumor, *HBPI* hepatobiliary phase imaging, *ADC* apparent diffusion coefficient, *T1WI* T1-weighted imaging, *AP* arterial phase. Numbers in parentheses are percentages. Boxes with bold lines depict the subgroup of tumors with a high probability of classification in the corresponding tumor group. Other boxes are the remaining subgroups

AP in NET, target sign on HBP in ICC, and presence of septum in HCC (all $p < 0.001$). The sensitivity, specificity, and diagnostic accuracy of the CTA model for differentiating the five hypervascular tumors established in this study was 100%, 90.4%, and 99.4% for FNHs, 90.9%, 96.4%, and 96.1% for HCAs, 93.3%, 72.2%, and 82.8% for NETs, 88%, 91.1%, and 94.4% for ICCs, and 91.9%, 85.1%, and 93.0% for HCCs. Of 28 tumors with low SI on T1WI and iso or hyperintensity on ADC, 24 tumors were benign including FNHs ($n = 18$) and HCAs ($n = 6$). In our CTA model, six HCCs with neither septum nor capsule were misdiagnosed as non-HCC tumors including three scirrhous HCCs.

Discussion

Our study demonstrated that reverse target sign on HBP in FNHs, iso or hyperintensity on ADC maps for FNHs and HCAs, central hypointensity on AP for NETs, target sign on HBP for ICCs, and the capsule and septum for HCCs were independent and significant features for differentiating the five hypervascular primary hepatic tumors showing HBP hypointensity on gadoxetic acid MRI. In addition, our CTA model also revealed these imaging features were the first splitting factors in tandem with iso or hyperintensity on T1WI in HCA. Although HBP hypointensity is not considered to be the same as true washout, it is highly indicative of HCC in patients at risk of HCC [1, 23]. In the current study, we did not measure the diagnostic performance of classifying hepatic tumors based on conventional vascular profiles, as most of the tumors showed similar enhancement patterns. In that situation, clinical risk factors between HCC and non-HCC groups might influence decision making. However, in consideration of HCC developed via de-novo carcinogenesis, we focused only on imaging features. By applying distinguishing features for tumor classification derived from uni- and multivariate analysis, we achieved acceptable diagnostic accuracy (range 85.8–98.6%) for each tumor type.

In this study, the capsule and septum were distinguishable features of HCCs. Capsule and septum are well known characteristics of HCCs and are derived from expansive tumor growth. The capsule and septum are formed by condensation of fibrous elements of either surrounding noncancerous liver or tumor tissue with weaker growth activity compressed by adjacent tumor tissue with more aggressive growth, respectively [24, 25]. On gross pathology, capsule was observed in 93.2% and septum in 91.9% of HCCs. On imaging analysis, 83.8% of capsules and 79.7% of septa in HCCs were correctly identified. Among non-HCCs, capsule and septum appeared in six and two HCAs, respectively, leading to misclassification of three of these tumors as HCCs.

Ten HCAs (90.9%) and all FNHs (78.3%) showed iso or high ADC values as a strong distinguishable feature compared with HCC or ICC. Although FNHs and HCAs tend to show low ADC values as malignancy, some studies have demonstrated FNH and HCA showing iso or high

ADC values [25–27]. Although DWI characteristics of such tumors are not yet fully understood, based on reviews of surgically resected FNHs or HCAs, we surmise that abundant sinusoidal dilatation or congestion was responsible for high ADC values [16, 28]. In supporting that notion, 20 FNHs showed bright hyperintensity on T2WI, which is contradictory to general knowledge [19].

HBP is advantageous for delineating hypointense central scars against strongly enhanced tumor backgrounds in FNH [18, 29]. Prior studies, however, have described atypical FNHs as hypointense with or without peripheral rim enhancement on HBP (17–23% and 10–12%, respectively) [16, 17, 19, 30, 31]. Although there is no plausible explanation for this variable imaging feature of FNH, it is presumably associated with differences in OATP8 expression between the central area and peripheral rim [16]. In our study, such a reverse target sign was an independent predictor and the first splitting imaging feature on CTA for differentiating FNHs from other tumors. Although all 23 atypical FNHs were grossly hypointense on HBP, mimicking HCC, 19 (82.6%) accompanied peripheral thin hyperintense rims. Pathologic review of 13 surgically resected cases revealed a wide central area of congestion. This is responsible for hypointensity on HBP as well as T2 brightness.

Target sign on HBP, now considered an ancillary feature of ICC, was a distinguishing feature of hypervascular ICC, in line with prior studies [9, 13, 32]. Central enhancement is considered attributable to fibrosis, which has abundant interstitial space with or without necrosis [14, 32]. Although atypical, hypervascular ICC has been reported to have more cellular area with less fibrosis than typical rim-enhancing ICCs. Twenty-one ICCs (84.0%) in this study presented target sign, in agreement with a prior report [9].

Little is known about the characteristic imaging features of hepatic NETs. We found that the central hypointensity on AP was a discriminative feature from other tumors. NETs produce vasoactive hormones and fibrogenic substances, which affect tumoral hypervascularity and fibrotic tissue [33, 34]. Central defects could be explained by fibrosis on histologic analysis, which could be responsible for delayed enhancement on conventional dynamic imaging [33–35]. With only enhancement patterns, NET seemed to be the most difficult case to diagnose by differentiating from HCC as three NETs in our study were misclassified as HCCs. However, an intratumoral septum was not identified in any NETs, although four NETs had accompanying capsules.

There were certain limitations to our study. First, the retrospective study design with study samples selected based on subjective image analysis may have led to selection bias. Second, the unbalanced and heterogenous clinical risk factors among groups (high proportions of hepatitis B or C in the HCC group) might have led to bias in decision making because we did not confine HCC risk patients in consideration of HCC developed in noncirrhotic liver. Our results might be suffered from this limitation. However, we believe that this clinical scenario approximates real practice, as all study cases were under consideration for HCC when reviewing radiologic reports. Third, since not all tumors were surgically resected, the study might be afflicted by sampling error in distinguishing between FNHs and HCAs. In addition, we did not consider the subtype of HCA which can shows different imaging features on dynamic MR imaging. Fourth, since we considered multiple features derived from uni- and multivariate analysis, setting clear rules for reviewing imaging was difficult. Fifth, classification among the five categories of hepatic tumors might not be a clinical scenario.

In conclusion, ancillary MRI features established in our study can be helpful in the differentiation of hypervascular and hepatobiliary hypointense primary hepatic tumors on gadoxetic acid MRI.

Compliance with ethical standards

Conflict of interest The authors declare that they have no conflict of interest.

References

1. Neri E, Bali MA, Ba-Ssalamah A, Boraschi P, Brancatelli G, Alves FC, Grazioli L, Helmberger T, Lee JM, Manfredi R, Marti-Bonmati L, Matos C, Merkle EM, Op De Beeck B, Schima W, Skehan S, Vilgrain V, Zech C, Bartolozzi C (2016) ESGAR consensus statement on liver MR imaging and clinical use of liver-specific contrast agents. Eur Radiol 26:921-931. https://doi.org/10.1007/s00330-015-3900-3
2. Choi JY, Lee JM, Sirlin CB (2014) CT and MR imaging diagnosis and staging of hepatocellular carcinoma: part I. Development, growth, and spread: key pathologic and imaging aspects. Radiology 272:635-654. https://doi.org/10.1148/radiol.14132361
3. Lee YJ, Lee JM, Lee JS, Lee HY, Park BH, Kim YH, Han JK, Choi BI (2015) Hepatocellular carcinoma: diagnostic performance of multidetector CT and MR imaging-a systematic review and meta-analysis. Radiology 275:97-109. https://doi.org/10.1148/radiol.14140690
4. Hamm B, Staks T, Muhler A, Bollow M, Taupitz M, Frenzel T, Wolf KJ, Weinmann HJ, Lange L (1995) Phase I clinical evaluation of Gd-EOB-DTPA as a hepatobiliary MR contrast agent: safety, pharmacokinetics, and MR imaging. Radiology 195:785-792. https://doi.org/10.1148/radiology.195.3.7754011
5. Stern W, Schick F, Kopp AF, Reimer P, Shamsi K, Claussen CD, Laniado M (2000) Dynamic MR imaging of liver metastases with Gd-EOB-DTPA. Acta Radiol 41:255-262
6. Chen BB, Hsu CY, Yu CW, Wei SY, Kao JH, Lee HS, Shih TT (2012) Dynamic contrast-enhanced magnetic resonance imaging with Gd-EOB-DTPA for the evaluation of liver fibrosis in chronic hepatitis patients. Eur Radiol 22:171-180. https://doi.org/10.1007/s00330-011-2249-5
7. Ahn SS, Kim MJ, Lim JS, Hong HS, Chung YE, Choi JY (2010) Added value of gadoxetic acid-enhanced hepatobiliary phase MR

imaging in the diagnosis of hepatocellular carcinoma. Radiology 255:459-466. https://doi.org/10.1148/radiol.10091388
8. Motosugi U, Ichikawa T, Sou H, Sano K, Tominaga L, Muhi A, Araki T (2010) Distinguishing hypervascular pseudolesions of the liver from hypervascular hepatocellular carcinomas with gadoxetic acid-enhanced MR imaging. Radiology 256:151-158. https://doi.org/10.1148/radiol.10091885
9. Park HJ, Kim YK, Park MJ, Lee WJ (2013) Small intrahepatic mass-forming cholangiocarcinoma: target sign on diffusion-weighted imaging for differentiation from hepatocellular carcinoma. Abdom Imaging 38:793-801. https://doi.org/10.1007/s00261-012-9943-x
10. Yang K, Cheng YS, Yang JJ, Jiang X, Guo JX (2017) Primary hepatic neuroendocrine tumors: multi-modal imaging features with pathological correlations. Cancer Imaging 17:20. https://doi.org/10.1186/s40644-017-0120-x
11. Chung YE, Kim MJ, Kim YE, Park MS, Choi JY, Kim KW (2013) Characterization of incidental liver lesions: comparison of multidetector CT versus Gd-EOB-DTPA-enhanced MR imaging. PLoS One 8:e66141. https://doi.org/10.1371/journal.pone.0066141
12. Rimola J, Forner A, Reig M, Vilana R, de Lope CR, Ayuso C, Bruix J (2009) Cholangiocarcinoma in cirrhosis: absence of contrast washout in delayed phases by magnetic resonance imaging avoids misdiagnosis of hepatocellular carcinoma. Hepatology 50:791-798. https://doi.org/10.1002/hep.23071
13. Chong YS, Kim YK, Lee MW, Kim SH, Lee WJ, Rhim HC, Lee SJ (2012) Differentiating mass-forming intrahepatic cholangiocarcinoma from atypical hepatocellular carcinoma using gadoxetic acid-enhanced MRI. Clin Radiol 67:766-773. https://doi.org/10.1016/j.crad.2012.01.004
14. Jeong HT, Kim MJ, Chung YE, Choi JY, Park YN, Kim KW (2013) Gadoxetate disodium-enhanced MRI of mass-forming intrahepatic cholangiocarcinomas: imaging-histologic correlation. AJR Am J Roentgenol 201:W603-611. https://doi.org/10.2214/ajr.12.10262
15. Kang Y, Lee JM, Kim SH, Han JK, Choi BI (2012) Intrahepatic mass-forming cholangiocarcinoma: enhancement patterns on gadoxetic acid-enhanced MR images. Radiology 264:751-760. https://doi.org/10.1148/radiol.12112308
16. Fujiwara H, Sekine S, Onaya H, Shimada K, Mikata R, Arai Y (2011) Ring-like enhancement of focal nodular hyperplasia with hepatobiliary-phase Gd-EOB-DTPA-enhanced magnetic resonance imaging: radiological-pathological correlation. Jpn J Radiol 29:739-743. https://doi.org/10.1007/s11604-011-0624-4
17. Yoon JH, Kim JY (2014) Atypical Findings of Focal Nodular Hyperplasia with Gadoxetic Acid (Gd-EOB-DTPA)-Enhanced Magnetic Resonance Imaging. Iran J Radiol 11:e9269. https://doi.org/10.5812/iranjradiol.9269
18. Grazioli L, Bondioni MP, Haradome H, Motosugi U, Tinti R, Frittoli B, Gambarini S, Donato F, Colagrande S (2012) Hepatocellular adenoma and focal nodular hyperplasia: value of gadoxetic acid-enhanced MR imaging in differential diagnosis. Radiology 262:520-529. https://doi.org/10.1148/radiol.11101742
19. van Kessel CS, de Boer E, ten Kate FJ, Brosens LA, Veldhuis WB, van Leeuwen MS (2013) Focal nodular hyperplasia: hepatobiliary enhancement patterns on gadoxetic-acid contrast-enhanced MRI. Abdom Imaging 38:490-501. https://doi.org/10.1007/s00261-012-9916-0
20. Hwang YH, Lee SJ, Kang KY, Hur JS, Yee ST (2017) Immunosuppressive Effects of Bryoria sp. (Lichen-Forming Fungus) Extracts via Inhibition of CD8(+) T-Cell Proliferation and IL-2 Production in CD4(+) T Cells. J Microbiol Biotechnol 27:1189-1197. https://doi.org/10.4014/jmb.1701.01080
21. Ishigami K, Yoshimitsu K, Nishihara Y, Irie H, Asayama Y, Tajima T, Nishie A, Hirakawa M, Ushijima Y, Okamoto D, Taketomi A, Honda H (2009) Hepatocellular carcinoma with a pseudocapsule on gadolinium-enhanced MR images: correlation with histopathologic findings. Radiology 250:435-443. https://doi.org/10.1148/radiol.2501071702
22. Elsayes KM, Hooker JC, Agrons MM, Kielar AZ, Tang A, Fowler KJ, Chernyak V, Bashir MR, Kono Y, Do RK, Mitchell DG, Kamaya A, Hecht EM, Sirlin CB (2017) 2017 Version of LI-RADS for CT and MR Imaging: An Update. Radiographics 37:1994-2017. https://doi.org/10.1148/rg.2017170098
23. Choi SH, Byun JH, Lim YS, Yu E, Lee SJ, Kim SY, Won HJ, Shin YM, Kim PN (2016) Diagnostic criteria for hepatocellular carcinoma 3 cm with hepatocyte-specific contrast-enhanced magnetic resonance imaging. J Hepatol 64:1099-1107. https://doi.org/10.1016/j.jhep.2016.01.018
24. Kadoya M, Matsui O, Takashima T, Nonomura A (1992) Hepatocellular carcinoma: correlation of MR imaging and histopathologic findings. Radiology 183:819-825. https://doi.org/10.1148/radiology.183.3.1316622
25. Suh YJ, Kim MJ, Choi JY, Park YN, Park MS, Kim KW (2011) Differentiation of hepatic hyperintense lesions seen on gadoxetic acid-enhanced hepatobiliary phase MRI. AJR Am J Roentgenol 197:W44-52. https://doi.org/10.2214/ajr.10.5845
26. Chen ZG, Xu L, Zhang SW, Huang Y, Pan RH (2015) Lesion discrimination with breath-hold hepatic diffusion-weighted imaging: a meta-analysis. World J Gastroenterol 21:1621-1627. https://doi.org/10.3748/wjg.v21.i5.1621
27. Taouli B, Koh DM (2010) Diffusion-weighted MR imaging of the liver. Radiology 254:47-66. https://doi.org/10.1148/radiol.09090021
28. Grazioli L, Olivetti L, Mazza G, Bondioni MP (2013) MR Imaging of Hepatocellular Adenomas and Differential Diagnosis Dilemma. Int J Hepatol 2013:374170. https://doi.org/10.1155/2013/374170
29. An HS, Park HS, Kim YJ, Jung SI, Jeon HJ (2013) Focal nodular hyperplasia: characterisation at gadoxetic acid-enhanced MRI and diffusion-weighted MRI. Br J Radiol 86:20130299. https://doi.org/10.1259/bjr.20130299
30. Karam AR, Shankar S, Surapaneni P, Kim YH, Hussain S (2010) Focal nodular hyperplasia: central scar enhancement pattern using Gadoxetate Disodium. J Magn Reson Imaging 32:341-344. https://doi.org/10.1002/jmri.22262
31. Zech CJ, Grazioli L, Breuer J, Reiser MF, Schoenberg SO (2008) Diagnostic performance and description of morphological features of focal nodular hyperplasia in Gd-EOB-DTPA-enhanced liver magnetic resonance imaging: results of a multicenter trial. Invest Radiol 43:504-511. https://doi.org/10.1097/rli.0b013e3181705cd1
32. Joo I, Lee JM, Lee SM, Lee JS, Park JY, Han JK (2016) Diagnostic accuracy of liver imaging reporting and data system (LI-RADS) v2014 for intrahepatic mass-forming cholangiocarcinomas in patients with chronic liver disease on gadoxetic acid-enhanced MRI. J Magn Reson Imaging 44:1330-1338. https://doi.org/10.1002/jmri.25287
33. Bader TR, Semelka RC, Chiu VC, Armao DM, Woosley JT (2001) MRI of carcinoid tumors: spectrum of appearances in the gastrointestinal tract and liver. J Magn Reson Imaging 14:261-269
34. Woodard PK, Feldman JM, Paine SS, Baker ME (1995) Midgut carcinoid tumors: CT findings and biochemical profiles. J Comput Assist Tomogr 19:400-405
35. Kim JE, Lee WJ, Kim SH, Rhim H, Song HJ, Park CK (2011) Three-phase helical computed tomographic findings of hepatic neuroendocrine tumors: pathologic correlation with revised WHO classification. J Comput Assist Tomogr 35:697-702. https://doi.org/10.1097/rct.0b013e318231c6d8